Marín-Suárez, Marco; Pashkin, Yuri A.; Peltonen, Joonas T.; Pekola, Jukka P.

Suppression of Back-Tunneling Events in Hybrid Single-Electron Turnstiles by Source-Drain Bias Modulation

Published in:
Physical Review Applied

DOI:
10.1103/PhysRevApplied.19.044088

Published: 01/04/2023

Document Version
Publisher's PDF, also known as Version of record

Suppression of Back-Tunneling Events in Hybrid Single-Electron Turnstiles by Source-Drain Bias Modulation

Marco Marín-Suárez,[1,*,†] Yuri A. Pashkin,[2] Joonas T. Peltonen,[1] and Jukka P. Pekola[1]

[1] *Pico group, QTF Centre of Excellence, Department of Applied Physics, Aalto University, Aalto FI-000 76, Finland*

[2] *Department of Physics, Lancaster University, Lancaster LA1 4YB, United Kingdom*

(Received 14 October 2022; revised 28 November 2022; accepted 29 March 2023; published 27 April 2023)

The accuracy of single-electron currents produced in hybrid turnstiles at high operation frequencies is, among other errors, limited by electrons tunneling in the wrong direction. Increasing the barrier transparency between the island and the leads, together with the source-drain bias, helps to suppress these events in a larger frequency range, although they lead to some additional errors. We experimentally demonstrate a driving scheme that suppresses tunneling in the wrong direction, thus extending the range of frequencies for generating accurate single-electron currents. The main feature of this approach is an additional ac signal applied to the bias with frequency twice that applied to the gate electrode. This allows additional modulation of the island chemical potential. By using this approach under certain parameters, we improve the single-electron current accuracy by one order of magnitude. Finally, we show through experimentally contrasted calculations that our method can improve accuracy even in devices for which the usual gate driving gives errors of the order of 10^{-3} at high frequencies and can bring them under 5×10^{-4}.

DOI: 10.1103/PhysRevApplied.19.044088

I. INTRODUCTION

Since the revision of the Système International d'Unités [1], quantum devices have been used for realizations of base units in terms of fundamental physical constants, especially in the electrical domain [2–5]. For current standard implementations, mainly single-electron transport experiments have been carried out [6–8]. In particular, *S-I-N-I-S* (*S* stands for superconductor, *I* for insulator, *N* for normal metal) single-electron turnstiles (SETs) have been widely implemented as sources of stable dc currents [9], among other applications [10–12] including a power standard [13]. In order to provide a reliable standard for the ampere, accuracy in generating a current $I = ef$, where e is the elementary charge and f the turnstile operation frequency, is needed, in addition to high magnitude (at least 100 pA). Deviations from the desired current arise from tunneling errors such as missed tunneling events [14], two-electron Andreev reflection [15,16], inelastic cotunneling [17], quasiparticle poisoning [11,12,18–20], and junction subgap leakage [21–24], among other photon-assisted processes due to the effect of the electromagnetic environment [25].

In the past, many proposals to minimize these errors have been put forward, mainly through device engineering. Superconducting quasiparticle poisoning has been reduced by changing the lead geometry and superconducting energy gap engineering [11,26,27], among other things [12,18]. Efforts to correct missed tunneling events have been directed towards error counting [14,28–30]. Andreev tunneling can be suppressed by increasing the island charging energy E_c so that it is larger than the energy gap Δ of the leads, or by increasing the tunnel junction resistance [15,31]. Furthermore, proper engineering of the electromagnetic environment has been proved to reduce the junction subgap leakage [32,33] and proposed for suppressing inelastic cotunneling [34]. One additional important error is the tunneling of electrons in the direction opposite to the bias voltage [13]. These undesired events give $I < ef$ and appear when the amplitude of the driving signal is large enough and its rate of change (proportional to f) is comparable to the device response scale. Typical approaches to avoid these events include decreasing either the total tunnel resistance of the device R_T or E_c; however, this may result in an enhancement of two-electron Andreev events. Furthermore, increasing the dc source-drain bias voltage also helps to suppress these events, but at the same time promotes subgap leakage current. As an alternative, in the present work we demonstrate and justify a different driving method that extends the useful driving frequency

*marco.marinsuarez@meetiqm.com
†Current address: IQM Finland OY.

range of a *S-I-N-I-S* SET by suppressing electron tunneling in the wrong direction and favors desired events. Our approach mainly involves adding a periodic modulation to the source-drain bias synchronized with the gate voltage modulation.

Our method effectively modulates the rate at which the island chemical potential crosses the energy thresholds that trigger tunneling events. This allows the time window for tunneling to be increased, favoring the desired events and effectively blocking the unwanted ones. In particular, we slow down the evolution of energy difference for the desired processes while accelerating that of the unwanted events, hence decreasing the likelihood of the latter. Recently, a similar approach has been employed to suppress back-tunneling events in semiconductor quantum dot single-electron pumps [35], but with no bias modulation. With this, we go beyond the device and setup optimization for error suppression, turning our attention instead to modifying the island chemical potential evolution beyond the simple gate waveform modification.

This paper is organized as follows. In Sec. II we present the experimental methods used. In Sec. III we give the dc and ac characterization of the device under test. Next, in Sec. IV we present the physical reasoning behind our results. These results are then presented in Sec. V. Finally, in Sec. VI we present our conclusions.

II. EXPERIMENTAL METHODS

A. Fabrication

In order to put our alternative method into practice we fabricated the device shown in Fig. 1(a). The normal metal island [red in Fig. 1(a)] is made of copper and the superconducting leads [blue in Fig. 1(a)] are made of aluminum. We use electron-beam lithography (EBL; Vistec EBPG5000+ operating at 100 kV) for sample patterning and electron-beam metal evaporation for the metallization of the devices. We carry out the only EBL step on a Ge-based hard mask [36] deposited on top of a silicon-oxide-coated silicon wafer. This mask is composed of a 400-nm layer of poly(methyl methacrylate-methacrylic acid) [P(MMA-MAA)] covered by a 22-nm layer of Ge which is deposited by electron-beam evaporation, and there is a final top layer of poly(methyl methacrylate) (PMMA). In this patterning step, the small island and contacts of the *S-I-N-I-S* transistor are drawn together with large bonding pads and connections between these and the small features. For easier handling, the full 4-inch wafer is cut into smaller chips containing several devices. After development of the top PMMA layer, the pattern is transferred to the intermediate germanium layer by reactive ion etching in carbon tetrafluoride (CF_4). Next, inside the same chamber, the pattern is transferred to the bottom P(MMA-MAA) layer by anisotropic oxygen plasma etching. Immediately after this, an undercut profile is created

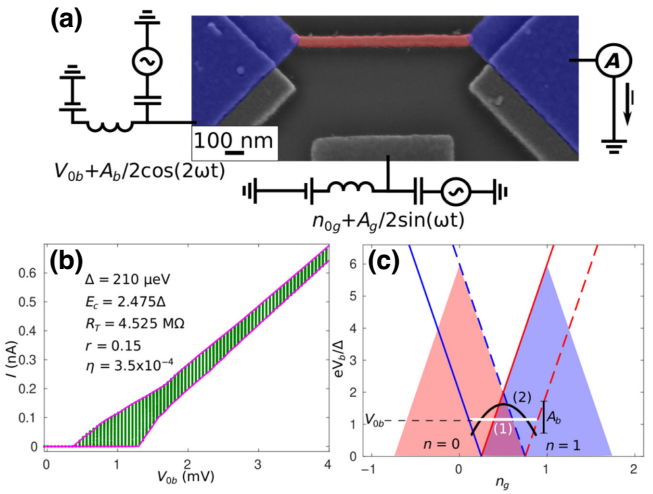

FIG. 1. (a) False-color electron micrograph with the measurement circuit used. Red is normal-metal, blue is superconductor. V_{0b}, dc bias voltage; A_b, peak-to-peak (p.p.) bias amplitude; n_{0g}, normalized dc gate-induced island charge; A_g, normalized p.p. gate charge amplitude; I, generated current; A, ammeter. (b) dc I-V curve. Green vertical lines are measured data within several gate periods and magenta lines are maximum and minimum current calculated with a Markovian model. (c) Top half of the stability diagram for a *S-I-N-I-S* SET with $r = 1$. Inside the Coulomb diamonds, ideally no current flows in the dc regime. The light red diamond corresponds to the island with excess charge $n = 0$ and the light blue diamond to $n = 1$. Lines are tunneling thresholds; blue (red) corresponds to right (left) junction, continuous (dashed) lines correspond to tunneling into (out of) the island. Crossing the line adds or removes one electron to or from the island. (1) corresponds to flat driving, (2) to parabolic driving.

by etching this layer with isotropic oxygen plasma. After this, we metallize the structure, first by depositing 20 nm of aluminum by electron-beam evaporation at an angle of 15.2° to form the leads. Inside the evaporation chamber, this layer is oxidized with 2.2 mbar of oxygen for 2 min. To create the island and finally form the *S-I-N-I-S* device, 30 nm of copper is deposited at an angle of −14.8°. The chip is then bathed in acetone to remove excess metal and the remaining P(MMA-MAA).

B. Measurements

After fabrication, the chip is cleaved to fit in a custom-made sample holder to which one device is bonded. This sample holder has been modified so that surface mounting inductors and capacitors form bias tees between dc and radio-frequency (rf) inputs, which are then connected to the sample gate and source electrodes by aluminum wires. The remaining drain electrode is connected to a dc line only. Direct current levels of the applied signals are injected through the bias tee inductors, while rf signals are injected through the bias tee capacitors. The sample holder

is then attached to the mixing chamber of a custom-made dilution refrigerator with a base temperature of approximately 100 mK. We apply dc signals through cryogenic lines composed of resistive twisted pairs running from room temperature down to the fridge 1 K flange and nearly 1 m of Thermocoax cable down to the mixing chamber. Radio-frequency signals were applied through the lines consisting of stainless steel coaxial cable installed between the room temperature (top) and 4.2 K flanges, a 20-dB attenuator at this temperature, followed by a feedthrough into the inner vacuum can inside which a NbTi coaxial cable follows from the 1 K flange down to the rf input of the holder. Additionally, at room temperature, 40 dB attenuation is applied to the line carrying the source-drain rf bias signal and a further 20 dB attenuator is connected to the gate rf line. We generate dc and ac signals by programmable voltage sources and waveform generators, respectively. To measure current, we use a digital multimeter for reading out the voltage in the output of the transimpedance current amplifier (FEMTO Messtechnik, model LCA-2-10T) connected to the device drain electrode through a dc line. To ensure proper synchronization and phase shift between the bias and gate rf signals, both were generated by a two-channel arbitrary waveform generator (Keysight, model 33522B). Each measurement of the pumped current was iterated typically 15 times and later averaged, ignoring those repetitions during which a charge offset jump had occurred. Then the offset of the current amplifier was subtracted by comparing the curves measured with biases of equal magnitude and opposite polarity.

III. DEVICE CHARACTERIZATION AND NEW PROPOSAL

Figure 1(b) shows the device dc current-voltage characteristics, which we measure by sweeping the dc gate voltage through about two gate periods for each dc bias voltage (green vertical lines). We calculate the maximum and minimum current using a Markovian equation (magenta lines; see Appendix for details on this model) with the following parameters: $\Delta = 210\ \mu\text{eV}$, $E_c = 2.48\Delta$, total normal-state tunnel resistance $R_T = 4.53\ \text{M}\Omega$, ratio between left and right junction tunnel resistances $r = 0.15$, and the Dynes parameter [37] $\eta = 3.5 \times 10^{-4}$. The I-V curves simulated with these parameters agree well with the measured data. The superconducting gap of the leads creates a bias-voltage zone inside of which, ideally irrespective of the gate voltage, no current flows [see Fig. 1(b)]. For biases $2\Delta < V_{0b} < 2\Delta + 2E_c$ current is suppressed only for certain gate voltages. These features create a diamondlike structure in the bias-voltage–gate-voltage parameter space inside of which the island charge remains stable. Figure 1(c) depicts two of these (only the upper half is shown) for states with zero and one extra electron in the island for a device with $r = 1$; notice how the diamonds overlap. These zones are bounded by the tunneling thresholds, which, if crossed, trigger a single-electron tunneling event between the island and one of the leads, either left (L) or right (R). These are defined by

$$\Delta = \pm 2E_c \left(n - n_g \pm 0.5\right) \pm eV_{b,L/R} \equiv \delta\epsilon^{\pm}_{L/R}. \quad (1)$$

We adopt the convention that positive biasing is from left (L) to right (R), hence $V_{b,L} = \kappa_L V_b$ and $V_{b,R} = -\kappa_R V_b$, where κ_i ($i = L, R$) is the ratio between the junction i capacitance and the total capacitance. Additionally, n is the initial island charge state. In Eq. (1) the plus signs indicate a tunneling event into the island and minus signs indicate events out of the island. The thresholds for $n = 0, 1$ are depicted in Fig. 1(c) (see its caption for further explanation). The key to the turnstile operation is to follow a path that crosses a threshold for electron tunneling into the island through one junction and then crosses another for a tunneling out of the island through the opposite junction without leaving the stability region. The most basic trajectory is depicted in Fig. 1(c) as path (1), henceforth called flat driving. Following this path back and forth with frequency f generates current $I = ef$ [9]. However, in Fig. 1(c) the curve designated as (2) is also suitable for generating dc currents. Such a path can be realized by adding an extra modulation to the bias such that

$$\begin{aligned} n_g &= n_{0g} + \frac{A_g}{2}\sin(\omega t), \\ V_b &= V_{0b} + \frac{A_b}{2}\cos(2\omega t), \end{aligned} \quad (2)$$

with $\omega = 2\pi f$. Considering time t as a parameter, Eq. (2) satisfies $V_b = V_{0b} + A_b/2 - 4\left(n_g - n_{0g}\right)^2 A_b/A_g^2$, that is, a parabola with negative concavity. Here, A_b is the peak-to-peak (p.p.) amplitude of the bias signal, A_g the p.p. amplitude of the gate signal, $n_g = C_g V_g/e$ with C_g the capacitance between the gate and the island, and V_g the voltage applied to the gate, in our device $C_g = 7.28$ aF. In practice, n_{0g} is set to the gate open position at the bottom of the parabola given by $n_{0g}^{\text{open}} = (V_{0b} - A_b/2)(r-1)/[4E_c(r+1)] + 0.5$, assuming $r = \kappa_R/\kappa_L$, which is a good approximation in this case. However, the choice of n_{0g} only affects the width of the current plateaus against A_g and whether or not certain ones appear. Notice that this path can be reduced to the flat one by setting $A_b = 0$. We have already employed a similar driving scheme [38] to show that single-electron currents can be generated by hybrid turnstiles at zero average bias. This was demonstrated for a wide range of bias amplitudes A_b, but always at $V_{0b} = 0$. While the novel charge pumping principle was implemented, we did not expect improvement of the pumping accuracy. Additionally, the turnstile was always operated at $n_{0g} = 0.5$.

The results of applying flat driving are depicted in Fig. 2 as dots along with calculations based on the same Markovian model used in the dc characterization and the same parameters, as solid lines. Our calculations carefully follow the dependence of the current against the driving amplitude for several biases, capturing deviations from the quantized current. Notice that for $f = 1$ MHz [Fig. 2(a)] $I \sim ef$ in a broad A_g interval (see inset), hence forming a clear plateau for most of the applied bias voltages except when excess events start to appear (for which $I > ef$). In contrast, for $f = 5$ MHz [Fig. 2(b)] these current plateaus bend down in a wide range of gate amplitudes such that $I < ef$ (see inset) and the accuracy decreases with increasing A_g until the next current plateau is reached. This occurs because when the driving amplitude increases, the parametric curve it traces crosses additional tunneling thresholds before reaching the next charge state. These thresholds allow tunneling events against the bias direction, referred to as back-tunneling events, which limit accuracy in Fig. 2(b). Such processes will only take place when the island has not been filled or emptied by the desired (forward) tunneling, which happens when the corresponding forward-tunneling rates are comparable to the inverse of the time elapsed between the crossings of the favorable and adjacent unfavorable thresholds; we denote this interval duration by δt. For continuous driving the extent of this time interval decreases with increasing frequency. There is an additional proportionality on V_{0b} whose form depends on the specific path and waveform; this is clearly shown in Fig. 2. Thus, in order to generate accurate single-electron current, one should increase δt. We propose that applying parabolic driving helps in this regard since it reshapes the quantities $\delta\epsilon^{\pm}_{L/R}$ so that the desired events cross the threshold at a lower rate and the undesired ones do so at a higher rate, thus increasing δt.

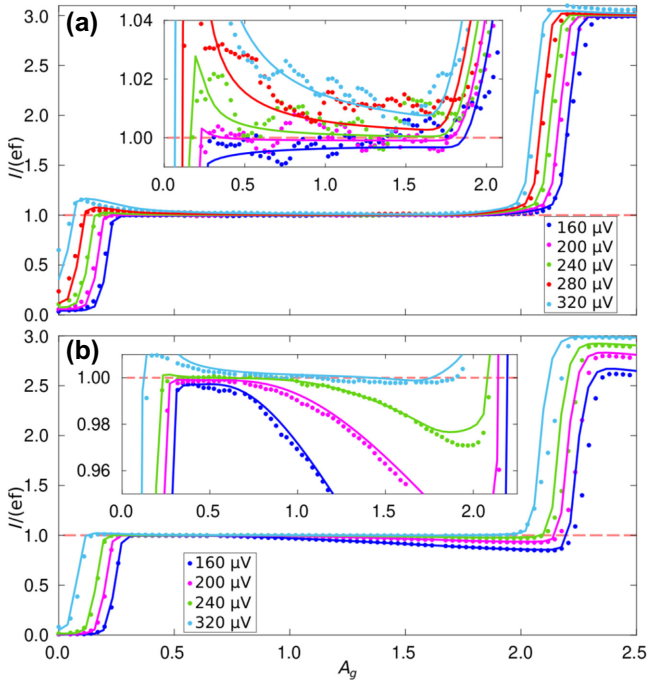

FIG. 2. (a) Typical single-electron current plateaus at $f = 1$ MHz with only dc bias. The legend shows the corresponding dc bias voltage V_{0b}. Dots are measured data, solid lines are simulations. Inset: zoom-in around $I/(ef) = 1$ showing the accuracy of the measured single-electron current and of our modeling. (b) As in (a) for $f = 5$ MHz. Note how the plateaus bend down, which is a clear signature of back-tunneling.

IV. EFFECT OF PARABOLIC DRIVING ON THE SYSTEM DYNAMICS

We clarify our proposition in this section by explaining how the parabolic protocol affects the island chemical potential evolution and what its impact is on back-tunneling events based on the Markovian model described in the Appendix. As shown there, the time evolution of the system is contained in $\delta\epsilon^{\pm}_{L/R}$ [Eq. (1)] through n_g and V_b. These quantities control the tunneling rates [Eq. (A2)], which, ideally, become nonzero only when $\delta\epsilon^{\pm}_{L/R} \geq \Delta$, that is, when the energy thresholds defining the stability diagram of an SET are crossed. We plot in Figs. 3(a) and 3(b) the evolution of $\delta\epsilon^{\pm}_{L/R}$ within one driving period τ, where each panel corresponds to one kind of the tunneling process (either out of [Fig. 3(a)] or into [Fig. 3(b)] the island) for both junctions. In the case of flat driving (solid lines),

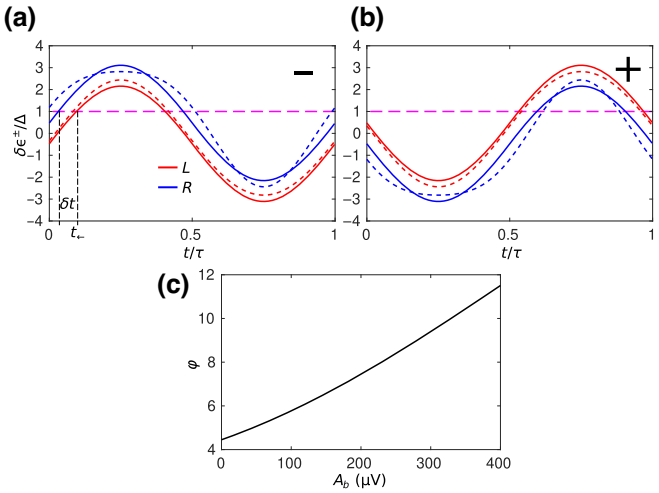

FIG. 3. (a) Time evolution of the system energy difference for single-electron tunneling out of the island in the flat protocol (solid lines) and in the parabolic protocol (dashed lines). Red indicates processes through the left junction, blue through the right, the magenta dashed line designates the tunneling thresholds, and τ is the period of the driving signal. (b) As in (a) for single-electron tunneling into the island. (c) Integral of the forward-tunneling rate against bias amplitude in the cases of (a) and (b).

the evolution is entirely controlled by the gate signal n_g and accordingly adopts its shape; we present the curves for $A_g = 1.06$ and $V_{0b} = 200$ μV. For parabolic driving (dashed lines), this evolution is also controlled by V_b, hence $\delta\epsilon^{\pm}_{L/R}$ adopts a different time evolution as compared to flat driving; in Fig. 3 we used $A_b = 240$ μV. The tunneling thresholds are depicted as magenta dashed lines in Fig. 3. Notice that the curve for the desired tunneling events ($\delta\epsilon^{-}_{R}$ and $\delta\epsilon^{+}_{L}$, in our particular case) crosses the threshold before the undesired ones ($\delta\epsilon^{-}_{L}$ and $\delta\epsilon^{+}_{R}$, in this case), whose crossings are only possible if the modulation amplitude is large enough. Hence, the former events will ideally happen first, making the latter ones impossible. However, if the time elapsed between the crossings of the two thresholds [δt in Fig. 3(a)] is too short, then the favorable event may not take place before the threshold crossing of the undesired event, therefore allowing the latter to occur. In the case of Fig. 3, there is clear back-tunneling for the flat driving when $f = 1/\tau = 5$ MHz [see Fig. 2(b)]. Notice how the use of the parabolic driving reshapes the curves and extends δt.

We show, based on a simplification of the model described in the Appendix, that by extending this time interval back-tunneling is suppressed. First, we simplify the model by assuming zero temperature, $T_N = T_S = 0$, and perfect junctions, $\eta = 0$. Under these conditions, the tunneling rates [Eq. (A2)] become

$$\Gamma\left(\delta\epsilon^{\pm}_{L/R}\right) = \frac{1}{e^2 R_{L/R}}\sqrt{\left(\delta\epsilon^{\pm}_{L/R}\right)^2 - \Delta^2}, \tag{3}$$

which is valid for $\delta\epsilon^{\pm}_{L/R} \geq \Delta$. In our particular case, the right junction, in so far as it is the less transparent one, sets the lower bound for back-tunneling, because tunneling rates through this junction are lower. Therefore, we focus on the events occurring through the right junction. We make a further approximation by stating that the probability of having one electron in the island at the time when the back-tunneling process energy crosses the threshold $t_{\leftarrow}$ [i.e., when $\delta\epsilon^{-}_{L} = \Delta$; see Fig. 3(a)] is [39]

$$p_1(t_{\leftarrow}) \approx \exp\left(-\int_{\delta t}\Gamma\left(\delta\epsilon^{-}_{R}\right)dt\right). \tag{4}$$

Having $p_1(t_{\leftarrow}) \ll 1$ means that the island has already been emptied before back-tunneling becomes energetically favorable, while $p_1(t_{\leftarrow}) \lesssim 1$ means that the island is not necessarily empty at $t_{\leftarrow}$ and hence it will likely be emptied through back-tunneling. Therefore, the larger the quantity $\varphi = \int_{\delta t}\Gamma\left(\delta\epsilon^{-}_{R}\right)dt$, the less likely back-tunneling is. In the case of Fig. 3(a), $\varphi_{\text{flat}} \approx 4.45$ for flat driving while $\varphi_{\text{par}} \approx 8.20$ for parabolic driving. Thus, we have $\varphi_{\text{par}} > \varphi_{\text{flat}}$. Hence, applying parabolic driving reduces the likelihood of back-tunneling events. Figure 3(c) shows that φ grows with A_b, therefore a larger bias amplitude suppresses back-tunneling more efficiently.

V. RESULTS AND DISCUSSION

A. Experimental results

We prove that the parabolic driving reduces the likelihood of back-tunneling experimentally by presenting the measured results for $f = 5$ MHz in Fig. 4 where back-tunneling has a strong influence on the current plateau. Figure 4(a) shows as dots the results of applying parabolic driving with $V_{0b} = 200$ μV for several bias amplitudes A_b. Note that the Markovian model agrees well with the measured current after applying a correcting factor of 2 to the amplitude of the ac signal delivered to the source electrode, which we deem as a result of the rf line transmittance [see the solid lines in Fig. 4(a)]. From these curves it is evident that the overall effect of the driving is to increase the current in the back-tunneling affected regime, a clear signature of back-tunneling suppression. These detrimental processes are replaced by forward-tunneling events which keep the current closer to the desired value $I = ef$ .Figure 4(b) shows the deviation from ideal $|I/(ef) - 1|$ of data in Fig. 4(a); notice that flat driving at $V_{0b} = 200$ μV gives a current accuracy of about 10^{-3} at best.

Instead, using a p.p. bias amplitude of 100 μV, 180 μV, and 240 μV lowers the deviation to the 10^{-4} level. A depiction of the paths followed in the stability diagram of the measured device can be seen in Fig. 4(c). From there it is clear that for larger A_b the path length between the threshold crossings for desired and undesired events increases. For $V_{0b} = 100$ μV the improvement is more drastic [see Figs. 4(d) and 4(e)]. The minimum deviation achieved with flat driving exceeds 10^{-2}, while it is at the level of 10^{-3} and even below for a narrow interval of gate amplitudes for $A_b = 400$ μV; Fig. 4(f) shows the paths followed. Furthermore, for most of the plateau the error even exceeds 10^{-1} in the first case, while in the second it remains below 10^{-2} for a wide A_g interval. This demonstrates that even for the conditions in which accuracy is otherwise poor we can increase it by one order of magnitude or more using the extra bias modulation. In Fig. 4(d) we can see that the maximum current (against A_g) decreases with increasing A_b before starting to increase. Interestingly, this happens in the gate amplitude interval where back-tunneling is not energetically favorable. According to our model, this effect is due to an interplay between the reshaping that the protocol causes on $\delta\epsilon^{\pm}_{L/R}$ and the subgap states in the superconducting leads (leakage). Because of these, tunneling is possible even when $\delta\epsilon^{\pm}_{L/R} < \Delta$, though with lower rates. In general, parabolic driving increases the maxima of these quantities for undesired tunneling while decreasing them for desired events. Therefore, back-tunneling subgap rates increase while the forward-tunneling ones decrease and current decreases.

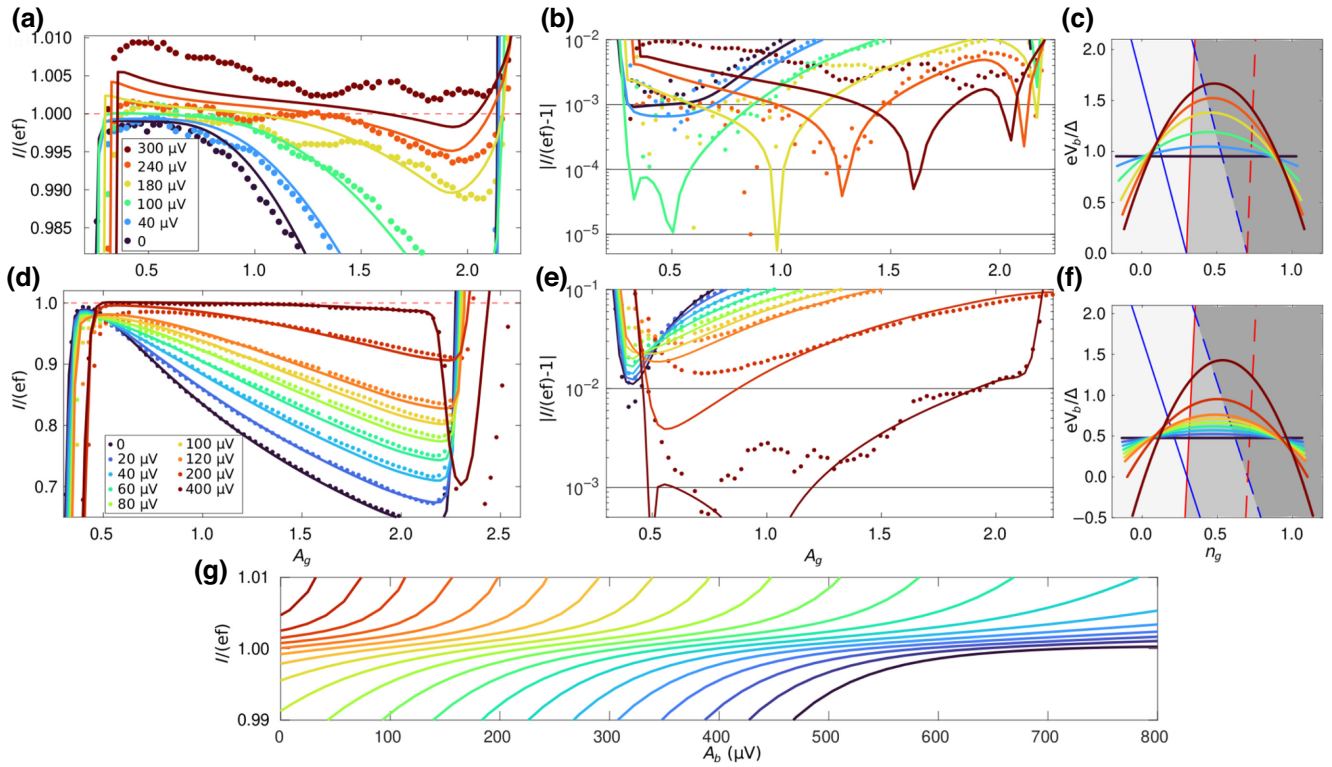

FIG. 4. (a) Current plateaus using parabolic driving at $f = 5$ MHz and $V_{0b} = 200$ μV; the legend designates the p.p. bias amplitude used. Dots represent measurements, solid lines simulations. (b) Deviation from ideal $|I/(ef) - 1|$ of data and calculations of (a) with the same legend. (c) Depiction of the protocols used in the n_g–V_b space. Colors correspond to the curves of (a) and (b). The stability diagram corresponds to the estimated parameters of the measured device. It has been zoomed in to the intersection between charge states for clarity. Tunneling thresholds correspond to the convention of Fig. 1(c). (d) Measured current plateaus using the proposed protocol at $f = 5$ MHz and $V_{0b} = 100$ μV; the legend designates the p.p. bias amplitude used. (e) As in (b), corresponding to (d). (f) As in (c), corresponding to (d) and (e). (g) Current calculated at the plateau ($A_g = 1.2$) as a function of the p.p. bias amplitude of the parabolic protocol; curves from right to left go from $V_{0b} = 0$ to 360 μV in steps of 20 μV.

This imbalance is accentuated with increasing A_b and is only important as long as the forward-tunneling thresholds are not crossed. Such an effect is minimized with better junctions having a lower Dynes parameter.

To understand how the current at the plateaus varies with A_b, we plot the former against the latter in Fig. 4(g). These curves have been calculated with a constant $A_g = 1.2$. We see that even for $V_{0b} = 0$ our measured protocol can recover the expected current for large enough A_b. However, the higher the dc bias, the more sensitive to the bias amplitude the current becomes. In any case the current tends to converge around the ideal value, although not with the same robustness as against A_g or V_{0b}. Ideally, one expects the current not to depend very strongly on A_b around ef in order to have a good standard, therefore one would expect to see plateaus against this parameter.

B. Future prospects

We use our theoretical model to evaluate how promising parabolic driving is. For this, we simulate the turnstile operation for a device with $\Delta = 200$ μeV, $E_c = 1.2\Delta$, $R_T = 200$ kΩ, $\eta = 10^{-6}$, and $r = 1$. These parameters ensure that the turnstile produces accurate single-electron currents for driving at high frequency. Furthermore, we set the island temperature to $T_N = 10$ mK and the leads temperature to $T_{L/R} = 100$ mK, which corresponds to a good quasiparticle relaxation. These are realistic device characteristics that can be routinely obtained with dedicated fabrication and setup conditioning [11,22]. In Fig. 5 we show the calculated current at operation frequency $f = 240$ MHz for which, ideally, $I \approx 38.45$ pA. It is clear that with flat driving, even though certain biases are subject to back-tunneling except for $V_{0b} = 280$ μV and $V_{0b} = 320$ μV, accurate single-electron current emission is achievable with plateaus ranging between 10^{-4} and 10^{-3} deviation [see Figs. 5(a) and 5(b)]. It is also evident that the application of parabolic driving with $V_{0b} = 200$ μV and $A_b = 250$ μV increases the accuracy of the current compared to flat driving when the same dc bias level is applied since it dramatically reduces back-tunneling. Moreover, the current produced with the new protocol is clearly more

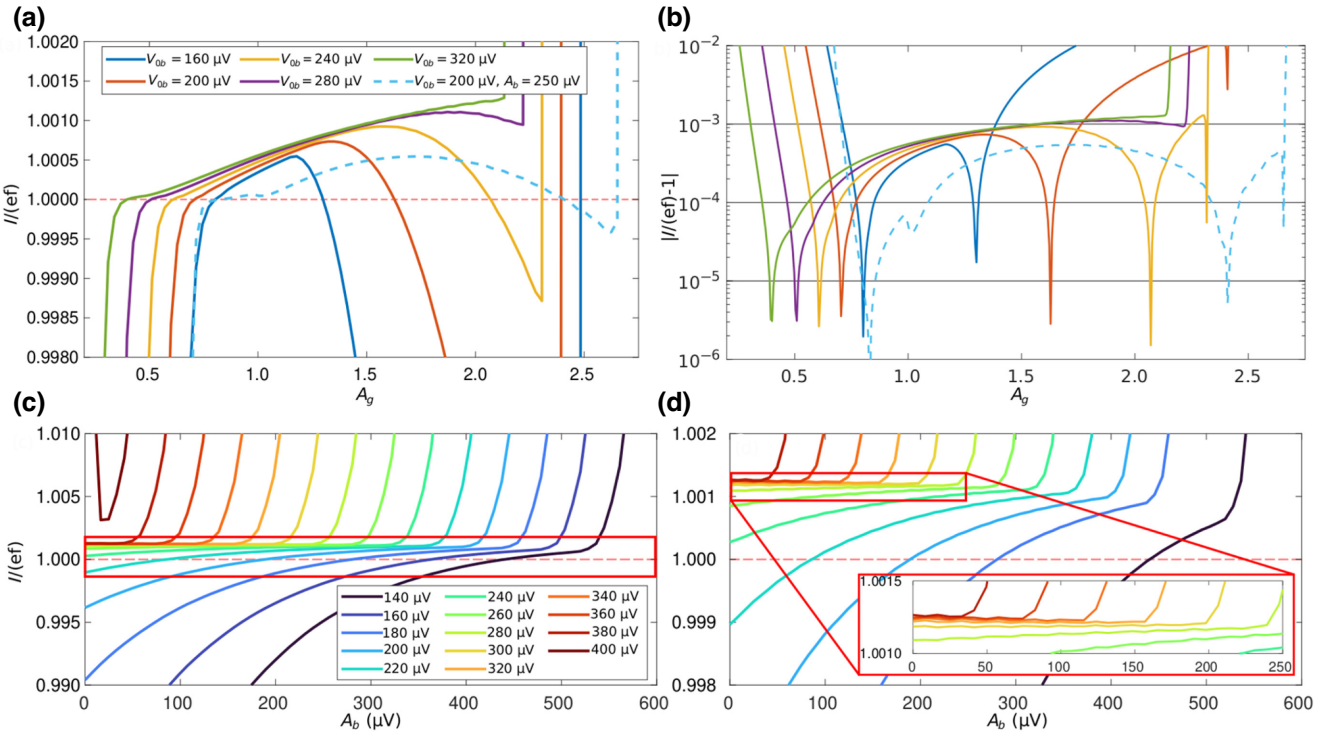

FIG. 5. (a) Simulated current plateaus. The legend shows the biasing conditions for the flat protocol. The dashed line was calculated using the parabolic protocol with the amplitude given in the legend. (b) Deviation of current in (a) with the same legend. (c) Calculated current at the plateau ($A_g = 2.0$) against the protocol amplitude A_b. The legend indicates the V_{0b} used. (d) Zoom-in of the enclosed area of (c). Inset: zoom-in of the enclosed area.

accurate than any other presented in Fig. 5(a). In fact, although the crossing of the level $I = ef$ causes the deviations to go below even 10^{-5} for flat driving, we get a broader region for which the error falls below 10^{-4} and 10^{-3} when using our alternative approach. Additionally, the implementation of our method improves the flatness of the plateau. Figure 5(c) shows the behavior of the current against A_b for several values of V_{0b} at $A_g = 2$. We can see that the robustness of the plateaus improves compared to Fig. 4(g). Furthermore, for certain dc bias values the current remains very much constant [see Fig. 5(d) and inset] although for these there is generally no discernible improvement in current accuracy when employing the new method ($A_b \neq 0$). The observed excess current which drives the deviation to about 10^{-3} is due to remaining two-electron tunneling errors caused by Andreev reflection. However, we ascribe the reduction of excess current in Fig. 5(a) to a reduction of Andreev reflection, although we do not claim this to be a generic effect of parabolic driving on single-electron current generation, which is beyond the scope of this work.

Further implementations of SET driving procedure with bias modulation could include a phase shift of this signal by π, inverting the parabola. This would decrease the time window for forward tunneling only; however, it could also reduce the current leakage. We would like to stress that, all in all, the use of any kind of modified driving protocol involving bias modulation alters the rate at which $\delta\epsilon^{\pm}_{L/R}$ passes the tunneling thresholds while keeping the operation frequency. Thus, these strategies can be used to improve the accuracy of frequency-to-power conversion of Ref. [13] by reducing the threshold passing rate of the energies [39] while keeping the magnitude of generated power constant. Apparently, additional improvements are needed in order to attain the accuracy of 10^{-7} at the output currents of around 100 pA demonstrated in the semiconductor electron pumps with a tunable barrier [40,41]. These may include better protection from the environmental photons that promote leakage while allowing proper bias driving. Lower tunnel resistances are also necessary to maintain a wide frequency range free from back-tunneling errors while the inequality $E_c > \Delta$ holds, so that the unwanted tunneling events due to Andreev reflection are suppressed.

VI. CONCLUSIONS

In summary, we have, for the first time, tested a SET driving procedure involving bias modulation in a *S-I-N-I-S* device added to the commonly used periodic gate modulation. This second signal applied to the source electrode of the transistor has a frequency twice that of gate driving,

and an appropriate phase-locking with respect to it. Furthermore, we provided evidence of the advantage of using this scheme against the usual one under diverse conditions. We conclusively showed that the main effect of this alternative approach is the suppression of the tunneling events against the bias. These events compromise the accuracy of single-electron transport at high gate-driving frequencies. A Markovian description of the system, which accurately models the measured currents, supports our arguments for the superiority of the method employed here. We also showed that this driving procedure can be employed with noticeable improvement for a broad interval of source modulation amplitudes. Furthermore, based on the theoretical model, we maintained that our approach holds the promise of improving the accuracy in devices with optimized parameters at larger single-electron currents with respect to the usual driving procedure. This work opens up the path for testing new SET protocols other than gate driving alone. Many more driving methods can be implemented by modifying the waveforms used as well as the frequency and phase shift of the bias modulation.

ACKNOWLEDGMENTS

We acknowledge fruitful discussions with S. Kafanov. M.M.-S., J.T.P., and J.P.P. acknowledge support from Academy of Finland under Grant No. 312057. Yu.A.P. acknowledges support from the QSHS project funded by STFC.

APPENDIX A: MODEL DESCRIPTION AND NUMERICAL SIMULATIONS

1. General model

We described the *S-I-N-I-S* transistor dynamics using the Markovian model described in the Supplemental Material of Ref. [12]. Here we reproduce this explanation with modifications pertinent to the present study.

We model the dynamics of a single-electron transistor from a stochastic master equation for the number of excess charges in the island n. The probability of having n excess electrons (also referred to as the state n), $p\,(n)$, evolves as [42–45]

$$\frac{d}{dt}p\,(n,t) = \sum_{n'\neq n} \gamma_{n'n} p\left(n',t\right) - \gamma_{nn'} p\,(n,t), \tag{A1}$$

where $\gamma_{nn'}$ is the total transition rate of the system for going from state n to n'. In the specific case of an SET, the transition rates are given by $\gamma_{nn'} = \Gamma^{L}_{n\to n'} + \Gamma^{R}_{n\to n'}$. Here, $\Gamma^{L/R}_{n\to n'}$ is the transition rate between individual charge states n and n' due to tunneling through either the left (L) or the right (R) junction.

We restrict the model to single-electron tunneling and two-electron Andreev reflection. In a *N-I-S* junction the rates for these processes are given by

$$\Gamma^{L/R}_{n\to n\pm1}\left(\delta\epsilon^{\pm}_{L/R}\right) = \frac{1}{e^2R_T}\int dE\, n_S\left(E-\delta\epsilon^{\pm}_{L/R}\right) f_N\,(E) \times\left[1-f_S\left(E-\delta\epsilon^{\pm}_{L/R}\right)\right] \tag{A2}$$

for single-electron tunneling, and

$$\Gamma^{L/R}_{n\to n\pm2}\left(\delta\epsilon^{\pm2}_{L/R}\right) = \frac{\hbar\Delta^2}{16\pi e^4R_T^2\mathcal{N}}\int dE f_N\left(E+\delta\epsilon^{\pm2}_{L/R}/2\right) \times f_N\left(-E+\delta\epsilon^{\pm2}_{L/R}/2\right) \times\left|a\,(E+E_c-i\xi/2)+a\,(-E+E_c-i\xi/2)\right|^2 \tag{A3}$$

for Andreev tunneling. For the case of Eq. (A2) $\delta\epsilon^{\pm}_{L/R}$ is given in Eq. (1), and for Eq. (A3)

$$\delta\epsilon^{\pm2}_{L/R} = \pm4E_c\left(n-n_g\pm1\right)\pm2eV_{b,L/R}. \tag{A4}$$

Here $V_{b,L}=\kappa_L V_b$ and $V_{b,R}=-\kappa_R V_b$, $\kappa_{L/R}$ is the ratio between the junction capacitance and the total capacitance, V_b is the bias voltage applied between the source-drain leads of the transistor, n is the initial island excess charge, n_g is the charge number induced by the gate voltage, E_c is the charging energy, and $+\,(-)$ denotes tunneling to (from) the island.

In Eqs. (A2) and (A3), Δ is the superconducting gap of the leads, R_T is the tunnel resistance of the junction involved in the event, and $\mathcal{N}$ is the number of conduction channels which can be written as $A/A_{\rm ch}$, with A being the junction area (around 50 nm × 60 nm for the present device) and $A_{\rm ch}$ is the area of an individual channel, estimated to be 30 nm^2, although this precise value does not affect the results of the model in the present case since $E_c>\Delta$ [15]. The term ξ takes into account the energy of the intermediate (single-electron tunneling) state which has a finite lifetime and correspondingly can be calculated as $\hbar\sum_{\pm}\Gamma_{n\to n\pm1}$ [17]; for the present case we use $\xi/\Delta=10^{-5}$. For our purposes, the exact value of this quantity does not have an impact on the value of the rates [46]. Additionally, f_N is the Fermi-Dirac distribution function for electrons in the normal-metal island, f_S is that for the superconducting lead involved in the tunneling event, and n_S is the superconducting density of states given by [47],

$$n_S\,(E) = \left|\mathrm{Re}\left(\frac{E/\Delta+i\eta}{\sqrt{(E/\Delta+i\eta)^2-1}}\right)\right|. \tag{A5}$$

Here η is the Dynes parameter that helps model subgap leakage [37]. Finally,

$$a(x) = \frac{1}{\sqrt{x^2-\Delta^2}} \ln\left(\frac{\Delta - x + \sqrt{x^2-\Delta^2}}{\Delta - x - \sqrt{x^2-\Delta^2}}\right). \quad \text{(A6)}$$

In our work we have measured the SET in two different regimes, namely the dc and turnstile operations.

2. Direct current operation

To calculate the current through the SET as a response to applied dc bias (V_b) and gate voltages (V_g) through $n_g = C_g V_g/e$, we solve Eq. (A1) in the steady state, that is, $dp(n,t)/dt = 0$. Since the charge states n are discrete, one can express Eq. (A1) as a matrix equation

$$A\mathbf{p} = \mathbf{0}, \quad \text{(A7)}$$

where $p_n = p(n)$, $A_{nn} = -\sum_{n' \neq n} \gamma_{nn'}$, and $A_{nn'} = \gamma_{nn'}$ for $n \neq n'$. Hence, the steady-state probability of having n electrons in the island is found by calculating the null space of A.

In order to get accurate results in the dc regime, heating of the island due to nonzero power dissipation has to be taken into account. To do this, we need to calculate the total power transferred to the normal-metal island in the steady-state regime using a vector $\mathbf{q}$ such that $q_n = \dot{Q}^N_{n\to n+1} + \dot{Q}^N_{n\to n-1}$ with $\dot{Q}^N_{n\to n\pm1} = \dot{Q}^{N,R}_{n\to n\pm1} + \dot{Q}^{N,L}_{n\to n\pm1}$, where

$$\dot{Q}^{N,L/R}_{n\to n\pm1}\left(\delta\epsilon^{\pm}_{L/R}\right) = \frac{1}{e^2 R_T}\int dE\, E n_S\left(E - \delta\epsilon^{\pm}_{L/R}\right) f_N(E) \times\left[1 - f_S\left(E - \delta\epsilon^{\pm}_{L/R}\right)\right], \quad \text{(A8)}$$

that is, the power transferred by the electron tunneled in a single event. Also, $\delta\epsilon^{\pm}_{L/R}$ is the related energy cost of single-electron tunneling defined by Eq. (1). Then the total power transferred to the island is $\dot{Q} = \mathbf{q}\cdot\mathbf{p}$. This power is dissipated by electron-phonon interaction [48] creating an equilibrium state in which the phonon temperature T_0 (which is taken as the temperature of the bath) differs from the temperature of the island electron system T_N. These temperatures depend on the power dissipated as $\dot{Q}_{e\text{-ph}} = \mathcal{V}\Sigma\left(T_N^5 - T_0^5\right)$, where $\mathcal{V}$ is the volume of the island and Σ is the electron-phonon coupling constant (approximately 8.4×10^9 W K^{-5} m^{-3} for copper, which was obtained in earlier experiments [13]). An additional power transfer due to Andreev reflection is considered in the form of Joule heat, that is, $\dot{Q}_A = \langle I_A\rangle V_b$ [49], where I_A is the current due only to Andreev events and V_b is the applied bias voltage. Finally, the heat balance is $\dot{Q}_{e\text{-ph}} = \dot{Q} + \dot{Q}_A$, in the present case $\dot{Q}_A \sim 0$. Notice that the transition rates depend also on T_N. Hence, this quantity has to be solved for self-consistently to satisfy Eq. (A7) and the heat balance.

Once T_N is determined with sufficient accuracy (for this we set a tolerance of 0.01 mK), Eq. (A7) can be solved for $\mathbf{p}$. Then the current through the SET I can be calculated as

$$I = \mathbf{b}\cdot\mathbf{p}, \text{ where}$$
$$b_n = e\left(\Gamma^L_{n\to n+1} - \Gamma^L_{n\to n-1}\right) + 2e\left(\Gamma^L_{n\to n+2} - \Gamma^L_{n\to n-2}\right). \quad \text{(A9)}$$

3. Turnstile operation

To model the turnstile operation we cannot use Eq. (A7). Instead we have

$$\frac{d}{dt}\mathbf{p}(t) = A(t)\,\mathbf{p}(t). \quad \text{(A10)}$$

The time dependence of matrix A stems from the time dependence of $\delta\epsilon^{\pm}_{L/R}$, which, in turn, is contained in n_g for flat driving and additionally in V_b for parabolic driving [see Eqs. (2) in the main text].

To calculate the current, we propose an evolution equation for the state averaged charge in the island $\langle q\rangle_s$ [45],

$$\frac{d}{dt}\begin{bmatrix}\mathbf{p}(t)\\ \langle q\rangle_s(t)\end{bmatrix} = \begin{bmatrix}A(t) & \mathbf{0}\\ \mathbf{b}(t)^T & 0\end{bmatrix}\begin{bmatrix}\mathbf{p}(t)\\ \langle q\rangle_s(t)\end{bmatrix}. \quad \text{(A11)}$$

Notice that Eq. (A11) includes Eq. (A9).

The solutions of Eq. (A11) are given by

$$\begin{bmatrix}\mathbf{p}(t)\\ \langle q\rangle(t)\end{bmatrix} = \exp\left(\int_0^t dt'\begin{bmatrix}A(t') & \mathbf{0}\\ \mathbf{b}(t')^T & 0\end{bmatrix}\right)\begin{bmatrix}\mathbf{p}(0)\\ \langle q\rangle(0)\end{bmatrix}. \quad \text{(A12)}$$

In the specific operation of the single-electron turnstile, one assumes periodic boundary conditions for $\mathbf{p}$ with the same period as n_g, the driving signal. This is reasonable since the tunneling rates have the same periodicity as this signal. Therefore, one can approximate the integral by discretizing the driving cycle of period τ into m intervals of size $\delta\tau = \tau/m$. At the end of the period the exponential is then

$$\tilde{U}(\tau) = \prod_{k=1}^{m}\exp\left(\delta\tau\begin{bmatrix}A(t_k) & \mathbf{0}\\ \mathbf{b}(t_k)^T & 0\end{bmatrix}\right), \quad \text{(A13)}$$

where $t_k = (k-1)\delta\tau$.

We decompose this propagator as

$$\tilde{U}(\tau) = \begin{bmatrix} U(\tau) & \mathbf{0} \\ \mathbf{U}_b^T(\tau) & 0 \end{bmatrix}. \tag{A14}$$

Then we impose the boundary conditions in Eq. (A12) to get

$$\mathbf{p}(\tau) = \mathbf{p}(0) = U(\tau)\,\mathbf{p}(0). \tag{A15}$$

The calculation of $\mathbf{p}$ has been reduced to determining the eigenvector of $U(\tau)$ corresponding to the eigenvalue 1. Finally, we calculate the average charge according to Eq. (A12) as $\langle q\rangle(\tau) = \mathbf{U}_b(\tau)\cdot\mathbf{p}(0)$. As a result, the average current can be written as $I = \langle q\rangle(\tau)/\tau$.

[1] BIPM, Comptes rendus de la 26e réunion de la Conférence Générale des Poids et Mesures (2018).

[2] I. Y. Krasnopolin, R. Behr, and J. Niemeyer, Highly precise comparison of Nb/Al/AlO_x/Al/AlO_x/Al/Nb Josephson junction arrays using a SQUID as a null detector, Supercond. Sci. Technol. **15**, 1034 (2002).

[3] F. Hohls, A. C. Welker, C. Leicht, L. Fricke, B. Kaestner, P. Mirovsky, A. Müller, K. Pierz, U. Siegner, and H. W. Schumacher, Semiconductor Quantized Voltage Source, Phys. Rev. Lett. **109**, 056802 (2012).

[4] R. Ribeiro-Palau, F. Lafont, J. Brun-Picard, D. Kazazis, A. Michon, F. Cheynis, O. Couturaud, C. Consejo, B. Jouault, W. Poirier, and F. Schopfer, Quantum Hall resistance standard in graphene devices under relaxed experimental conditions, Nat. Nanotechnol. **10**, 965 (2015).

[5] M.-H. Bae, D.-H. Chae, M.-S. Kim, B.-K. Kim, S.-I. Park, J. Song, T. Oe, N.-H. Kaneko, N. Kim, and W.-S. Kim, Precision measurement of single-electron current with quantized Hall array resistance and Josephson voltage, Metrologia **57**, 065025 (2020).

[6] J. P. Pekola, O.-P. Saira, V. F. Maisi, A. Kemppinen, M. Möttönen, Yu. A. Pashkin, and D. V. Averin, Single-electron current sources: Toward a refined definition of the ampere, Rev. Mod. Phys. **85**, 1421 (2013).

[7] B. Kaestner and V. Kashcheyevs, Non-adiabatic quantized charge pumping with tunable-barrier quantum dots: A review of current progress, Rep. Prog. Phys. **78**, 103901 (2015).

[8] G. Yamahata, S. P. Giblin, M. Kataoka, T. Karasawa, and A. Fujiwara, Gigahertz single-electron pumping in silicon with an accuracy better than 9.2 parts in 10^7, Appl. Phys. Lett. **109**, 013101 (2016).

[9] J. P. Pekola, J. J. Vartiainen, M. Mötönen, O.-P. Saira, M. Meschke, and D. V. Averin, Hybrid single-electron transistor as a source of quantized electric current, Nat. Phys. **4**, 120 (2007).

[10] S. Kafanov, A. Kemppinen, Yu. A. Pashkin, M. Meschke, J. S. Tsai, and J. P. Pekola, Single-Electronic Radio-Frequency Refrigerator, Phys. Rev. Lett. **103**, 120801 (2009).

[11] H. S. Knowles, V. F. Maisi, and J. P. Pekola, Probing quasiparticle excitations in a hybrid single electron transistor, Appl. Phys. Lett. **100**, 262601 (2012).

[12] M. Marín-Suárez, J. T. Peltonen, and J. P. Pekola, Active quasiparticle suppression in a non-equilibrium superconductor, Nano Lett. **20**, 5065 (2020).

[13] M. Marín-Suárez, J. T. Peltonen, D. S. Golubev, and J. P. Pekola, An electron turnstile for frequency-to-power conversion, Nat. Nanotechnol. **17**, 239 (2022).

[14] J. T. Peltonen, V. F. Maisi, S. Singh, E. Mannila, and J. P. Pekola, On-chip error counting for hybrid metallic single-electron turnstiles, Preprint arXiv:1512.00374v1(2015).

[15] T. Aref, V. F. Maisi, M. V. Gustafsson, P. Delsing, and J. P. Pekola, Andreev tunneling in charge pumping with SINIS turnstiles, Europhys. Lett. **96**, 37008 (2011).

[16] V. F. Maisi, D. Kambly, C. Flindt, and J. P. Pekola, Full Counting Statistics of Andreev Tunneling, Phys. Rev. Lett. **112**, 036801 (2014).

[17] D. V. Averin and J. P. Pekola, Nonadiabatic Charge Pumping in a Hybrid Single-Electron Transistor, Phys. Rev. Lett. **101**, 066801 (2008).

[18] M. Taupin, I. M. Khaymovich, M. Meschke, A. S. Mel'nikov, and J. P. Pekola, Tunable quasiparticle trapping in Meissner and vortex states of mesoscopic superconductors, Nat. Commun. **7**, 10977 (2016).

[19] I. M. Khaymovich and D. M. Basko, Recovery of SINIS turnstile accuracy in a strongly nonequilibrium regime, Phys. Rev. B **94**, 165158 (2016).

[20] D. T. van Zanten, D. M. Basko, I. M. Khaymovich, J. P. Pekola, H. Courtois, and C. B. Winkelmann, Single Quantum Level Electron Turnstile, Phys. Rev. Lett. **116**, 166801 (2016).

[21] S. V. Lotkhov, A. Kemppinen, S. Kafanov, J. P. Pekola, and A. B. Zorin, Pumping properties of the hybrid single-electron transistor in dissipative environment, Appl. Phys. Lett. **95**, 112507 (2009).

[22] J. P. Pekola, V. F. Maisi, S. Kafanov, N. Chekurov, A. Kemppinen, Yu. A. Pashkin, O.-P. Saira, M. Möttönen, and J. S. Tsai, Environment-Assisted Tunneling as an Origin of the Dynes Density of States, Phys. Rev. Lett. **105**, 026803 (2010).

[23] O.-P. Saira, M. Möttönen, V. F. Maisi, and J. P. Pekola, Environmentally activated tunneling events in a hybrid single-electron box, Phys. Rev. B **82**, 155443 (2010).

[24] A. Kemppinen, S. V. Lotkhov, O.-P. Saira, A. B. Zorin, J. P. Pekola, and A. J. Manninen, Long hold times in a two-junction electron trap, Appl. Phys. Lett. **99**, 142106 (2011).

[25] A. Di Marco, V. F. Maisi, F. W. J. Hekking, and J. P. Pekola, Effect of photon-assisted Andreev reflection in the accuracy of a SINIS turnstile, Phys. Rev. B **92**, 094514 (2015).

[26] T. Yamamoto, Y. Nakamura, Yu. A. Pashkin, O. Astafiev, and J. S. Tsai, Parity effect in superconducting aluminum single electron transistors with spatial gap profile controlled by film thickness, Appl. Phys. Lett. **88**, 212509 (2006).

[27] J. T. Peltonen, A. Moisio, V. F. Maisi, M. Meschke, J. S. Tsai, and J. P. Pekola, Hybrid single-electron turnstiles with thick superconducting electrodes for improved quasiparticle relaxation, Preprint arXiv:1709.09832 (2017).

[28] M. Wulf, Error accounting algorithm for electron counting experiments, Phys. Rev. B **87**, 035312 (2013).

[29] L. Fricke, M. Wulf, B. Kaestner, F. Hohls, P. Mirovsky, B. Mackrodt, R. Dolata, T. Weimann, K. Pierz, U. Siegner, and H. W. Schumacher, Self-Referenced Single-Electron Quantized Current Source, Phys. Rev. Lett. **112**, 226803 (2014).

[30] D. Reifert, M. Kokainis, A. Ambainis, V. Kashcheyevs, and N. Ubbelohde, A random-walk benchmark for single-electron circuits, Nat. Commun. **12**, 285 (2021).

[31] A. Kemppinen, S. Kafanov, Yu. A. Pashkin, J. S. Tsai, D. V. Averin, and J. P. Pekola, Experimental investigation of hybrid single-electron turnstiles with high charging energy, Appl. Phys. Lett. **94**, 172108 (2009).

[32] S. V. Lotkhov, O.-P. Saira, J. P. Pekola, and A. B. Zorin, Single-charge escape processes through a hybrid turnstile in a dissipative environment, New J. Phys. **13**, 013040 (2011).

[33] V. Bubanja, Tunneling rates of electron pumping in the R-SINIS transistor, J. Low Temp. Phys. **175**, 564 (2014).

[34] V. Bubanja, Cotunneling suppression in a hybrid single-electron transistor by a dissipative electromagnetic environment, Phys. Rev. B **83**, 195312 (2011).

[35] F. Hohls, V. Kashcheyevs, F. Stein, T. Wenz, B. Kaestner, and H. W. Schumacher, Controlling the error mechanism in a tunable-barrier nonadiabatic charge pump by dynamic gate compensation, Phys. Rev. B **105**, 205425 (2022).

[36] M. Meschke, A. Kemppinen, and J. P. Pekola, Accurate Coulomb blockade thermometry up to 60 kelvin, Philos. Trans. R. Soc. A **374**, 20150052 (2016).

[37] R. C. Dynes, V. Narayanamurti, and J. P. Garno, Direct Measurement of Quasiparticle-Lifetime Broadening in a Strong-Coupled Superconductor, Phys. Rev. Lett. **41**, 1509 (1978).

[38] M. Marín-Suárez, Yu. A. Pashkin, J. T. Peltonen, and J. P. Pekola, Zero-average bias bidirectional single-electron current generation in a hybrid turnstile, J. Low Temp. Phys. **210**, 232 (2022).

[39] J. P. Pekola, M. Marín-Suárez, T. Pyhäranta, and B. Karimi, Ultimate Accuracy of Frequency to Power Conversion by Single-Electron Injection, Phys. Rev. Lett. **129**, 037702 (2022).

[40] F. Stein, D. Drung, L. Fricke, H. Scherer, F. Hohls, C. Leicht, M. Götz, C. Krause, R. Behr, E. Pesel, K. Pierz, U. Siegner, F. J. Ahlers, and H. W. Schumacher, Validation of a quantized-current source with 0.2 ppm uncertainty, Appl. Phys. Lett. **107**, 103501 (2015).

[41] F. Stein, H. Scherer, T. Gerster, R. Behr, M. Götz, E. Pesel, C. Leicht, N. Ubbelohde, T. Weimann, K. Pierz, H. W. Schumacher, and F. Hohls, Robustness of single-electron pumps at sub-ppm current accuracy level, Metrologia **54**, S1 (2016).

[42] I. O. Kulik and R. I. Shekhter, Kinetic phenomena and charge discreteness effects in granulated media, Zh. Eksp. Teor. Fiz. **68**, 623 (1975).

[43] K. K. Likharev and A. B. Zorin, Theory of the Bloch-wave oscillations in small Josephson junctions, J. Low Temp. Phys. **59**, 347 (1985).

[44] D. V. Averin and K. K. Likharev, Coulomb blockade of single-electron tunneling, and coherent oscillations in small tunnel junctions, J. Low Temp. Phys. **62**, 345 (1986).

[45] O.-P. Saira, Doctoral thesis, Aalto University, School of Science (2013). http://urn.fi/URN:ISBN:978-952-60-5076-8.

[46] V. F. Maisi, Doctoral thesis, Aalto University, School of Science (2014). http://urn.fi/URN:ISBN:978-952-6682-11-2.

[47] J. Bardeen, L. N. Cooper, and J. R. Schrieffer, Theory of superconductivity, Phys. Rev. **108**, 1175 (1957).

[48] F. C. Wellstood, C. Urbina, and J. Clarke, Hot-electron effects in metals, Phys. Rev. B **49**, 5942 (1994).

[49] S. Rajauria, P. Gandit, T. Fournier, F. W. J. Hekking, B. Pannetier, and H. Courtois, Andreev Current-Induced Dissipation in a Hybrid Superconducting Tunnel Junction, Phys. Rev. Lett. **100**, 207002 (2008).